Marangoni-driven spreading and receding of a volatile droplet on a liquid layer

Amin Jaberi, Gerald Debenest, Franck Plouraboué

Marangoni-driven spreading and receding of a volatile droplet on a liquid layer

Amin Jaberi, Gérald Debenest, and Franck Plouraboué
Institut de Mécanique des Fluides de Toulouse (IMFT), Université de Toulouse, CNRS, INPT, UPS, Toulouse 31400, France

(Received 15 December 2022; accepted 2 June 2023; published xxxxxxxxxx)

When releasing a droplet onto a distinct nonmiscible liquid layer, for positive spreading parameter S, a surface tension driven spreading arises. Here, for positive S, we report the reverse after the initial spreading phase: a secondary receding of the deposited volatile droplet. This behavior is found to result from the competition between two opposite effects: solutal and thermal Marangoni stresses, with the latter built from droplet's evaporation. To clarify the effects of evaporation-induced Marangoni, accurate infrared thermography tests are performed. These tests reveal a maximal temperature gradient at the droplet edge near the recession time. Also, universal scaling laws are proposed for the spreading dynamic of a law-viscous insoluble drop onto a more viscous oil, with droplet volume variation resulting from the evaporation and typical receding time. These predictions are successfully compared with experiments.

DOI: 10.1103/PhysRevFluids.00.003600

I. INTRODUCTION

Droplet interfacial dynamics over wetting solid substrates or liquid layers is a sophisticated phenomenon that has attracted much attention both because of its fundamental and practical interest [1]. It is relevant in many applicative contexts such as coating processes, inkjet printing, biocontamination, etc. In dynamical situations, the isothermal spreading of liquids produces complex dynamics associated with interfacial instabilities and fascinating pattern formations [2–7]. This spreading can also lead to a secondary instability of the interfacial front and beautiful fingering instability [8–10]. The spreading of a droplet after deposition on a liquid layer arises from a positive spreading coefficient, S [11],

$$S = \gamma_l - \gamma_d - \gamma_{ld}, \tag{1}$$

with γ_l, γ_d, and γ_{ld} being respectively the liquid layer/air, droplet/air, and liquid layer/droplet surface tension. It determines the energy per unit area of spreading, which is mostly balanced by the viscous forces in the liquid [12]. As opposed to these dynamical configurations, quasisteady ones such as evaporating sessile droplets have been studied where thermal Marangoni stress built from surface tension's dependence on temperature slightly deforms the interface, whereas creeping, convectively coupled evaporation flows are also observed [13].

Either from capillary forces acting at triple line associated with surface tension or from (solutal or thermal) dynamical Marangoni stress, the dynamics of droplet interfaces are governed by interfacial forces which can possibly play a synergetic role, or, on the contrary, an opposite one. Examples and illustrations of complex effects arising from interfacial forces at low Reynolds number are, in fact, numerous. An opposite effect is for an example found for the dewetting instability of a flat interface nearby a solid surface where capillary forces stabilize the interface from the action of Laplace pressure, but, at the same time, destabilize it from disjoining pressure. On the one hand, the physical system tries to minimize the air/liquid area favorable to a flat interface, while, on the other

hand, it is also favorable for creating a new solid/air interface (dewetting) for energy minimization. A synergetic effect is on the contrary known for an oil film spreading over a hot solid surface (the so-called "pan spreading" problem) both resulting from positive spreading coefficient and thermal Marangoni forces acting in the same direction eventually leading to a central dry spot [14].

When considering interfacial spreading onto a fluid layer, two distinct spreading mechanisms have been described [15]: Laplace spreading [16] and Marangoni spreading [12]. The first one has been found relevant for surface tension driven forces at triple line such as those arising for an oil drop deposited onto a much lower viscous deep liquid. In this case the spreading drop radius $R(t)$ dynamics display a power law $R(t) \sim (t/t_{cv})^n$, where t_{cv} is the capillary-viscous time (built upon the capillary length ℓ_c and the kinematic viscosity of the oil deposited drop, i.e., $t_{cv} = \ell_c^2/\nu_o$). Exponent n has been found experimentally in the range $n \in [0.25–0.4]$ [16], while the theoretical prediction for very deep layers is $n = 1/8 = 0.125$ [17]. Considering the distinct case of solutal driven monolayer spreadings either onto a single liquid [18,19] or at the interface between two liquids [12,15], the spreading mechanism arises from the coupled effect of Marangoni stress and Marangoni flow driving the solutal concentration dynamics at the interface. For this Marangoni spreading, a distinct spreading regime $R(t) \sim (t/t_{cv})^{3/4}$ has also been found. Recent experiments also found both regimes to happen depending on the relative importance of solutal Marangoni compared to Laplace spreading [15].

Here, we examine the spreading of a low viscous volatile liquid drop into a more viscous layer. For a volatile droplet, the induced thermal Marangoni force can indeed counteract the solutal ones. This was first studied by Keiser *et al.* [20], who experimentally investigate the flow dynamics of a water-IPA (isopropyl alcohol) mixture deposited on a thick layer of sunflower oil. Varying the mass fraction of water-IPA mixture, they reported a minimum concentration of IPA for which it spreads and fragments into a myriad of minuscule droplets. They also performed a scaling analysis to predict the spreading radius of the droplet, but their model failed to capture the self-similar behavior of the radius dynamic. Keiser *et al.* also used methylene blue to enhance the imaging contrast between IPA solution and substrate oil. In a subsequent study, Seyfert and Marin [21] performed experiments to examine the influence of this added dye on the Marangoni driven fingering instability. They found that increasing the concentration of methylene blue led to an increase in the instability wavelength. Keeping the same experimental configuration, Hasegawa and Manzaki [22] further explored the flow dynamics of an IPA droplet on sunflower oil. Measuring the temperature field, they reported a temperature gradient near the spreading front attributed to the induced thermal Marangoni stress after the first two seconds.

Despite these studies, there is still a lack of understanding regarding Marangoni-driven spreading of volatile droplets on an oil layer. Here, we report that the volatile drop deposited onto the oil layer experiences an outward motion that progressively slows down, stops, and finally reverses. To our knowledge, this recession of the deposited droplet has neither been reported, discussed, nor explained in previous studies.

The paper is organized as follows. Section II describes the various experimental setups and the calibration method for the optical measurements of the deposited droplet volume. Section III describes the experimental observations for the spreading dynamics, receding, and volume change, as well as the deposited edge temperature measurements. This section also analyzes the fingering instability. Section IV details the scaling analysis for the obtained spreading dynamics as well as its self-similar solution, further compared with measurements in Sec. V.

II. MATERIALS AND METHODS

A. Optical and thermal setups for the analysis of spreading dynamics

A schematic diagram of the experimental setup is presented in Fig. 1(a). This setup was used for all experiments, excluding infrared imaging. A 5 ml plastic syringe filled with methanol was put into an ExiGo microfluidic pump. The physical properties of the methanol are outlined in Table I.

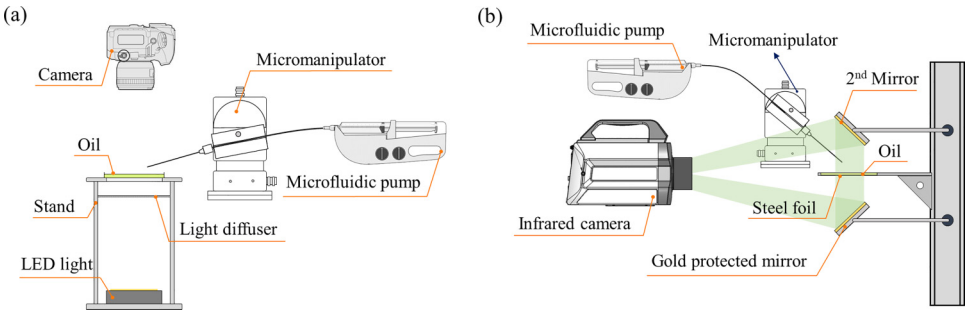

FIG. 1. Schematic illustrations of the experimental setup for (a) flow visualization tests and (b) infrared thermography tests. Experiments were performed in a room with controlled temperature and humidity.

Also, for providing a better visualization, methanol was colored with a 0.3 g/l volume concentration of methylene blue. To clamp the needle and precisely control its tip position, a Scientifica PatchStar micromanipulator was employed. A stand was utilized to hold an 88 mm diameter glass petri dish, which was filled with olive oil at different thicknesses ranging from 3 mm to 8 mm. The volume of oil was measured using a high precision balance (Mettler Toledo, ME3002). Before each test, the petri dish was emptied of any remnants from the previous test, carefully washed, and then dried. Four height controllers were used to ensure the stand was completely level. A diffused backlight imaging technique was implemented to visualize the liquid development. A high-lumen LED was placed beneath the diffuser to create a uniform bright background. Images were captured using a Nikon D850 camera equipped with a Micro Nikkor 105 mm lens. Once a droplet was released onto the oil surface, the needle was immediately removed from the field of view to avoid any optical shadowing or blockage. Taken photos were subsequently analyzed using an in-house image analysis program to identify the key characteristics of the liquid flow.

The main dimensionless numbers characterizing the physics of the problem are reported in Table II. Capillary number, Péclet number, and Reynolds number are tabulated for both methanol and olive oil. Also, the lubricated Reynolds number which is appropriate to quantify inertia effects within lubricated flow is provided [23]. To do so, the characteristic velocity of the methanol spreading was considered to be $U_m = 10$ mm/s (from experimental measurements). Using the tangential shear stress continuity condition along the methanol/oil interface provides the scaling $\mu_o U_o/H \sim \mu_d U_m/h_0$ and, for typical $H/h_0 \approx 20$, the characteristic velocity of oil is evaluated as $U_o \approx 2.4$ mm/s. The maximum thickness of the methanol droplet (h_0) holds a value around 10^{-4} m.

Considering the importance of thermal effects induced by the methanol evaporation, infrared thermography experiments were also conducted. Temperature field of the upper surface of the oil layer was most desired, but due to the physical limitations associated with direct thermography of a liquid surface, such measurements were not possible. To address this issue, we designed and

TABLE I. Physical properties of the methanol and olive oil.

Property	Symbol	Value (unit)
Methanol vapor pressure	p_v	13.02 (kPa)
Methanol density	ρ_d	792 (kg/m^3)
Methanol surface tension	γ_d	22.5 (mN/m)
Methanol viscosity	μ_d	5×10^{-4} (Pa s)
Olive oil density	ρ_o	917 (kg/m^3)
Olive oil surface tension	γ_o	32 (mN/m)
Olive oil viscosity	μ_o	0.084 (Pa s)

TABLE II. Main dimensionless numbers characterizing the physics of both methanol and oil flows. In the formulas, $\mathcal{H}$ stands for either the maximum thickness of methanol (h_0) or the olive oil height (H).

Number	Methanol	Olive oil
Capillary number Ca $= \mu U/\gamma$	2×10^{-4}	63×10^{-4}
Thermal Péclet number Pe $= \mathcal{H}U/\alpha$	19	89.3
Reynolds number Re $= \mathcal{H}U/\nu$	3.0	0.1
Lubricated Reynolds number (h_0/ℓ_c)Re	0.3	0.01

built a unique setup, as depicted schematically in Fig. 1(b). Accordingly, we used a double mirror configuration for reflecting thermal effects onto the infrared camera (FLIR X8501 sc). Both mirrors were held at the constant angle of 45°. Instead of a petri dish, the olive oil was poured into a polymer ring with a 0.05 mm thick steel foil as the bottom surface. The exterior surface of the foil was painted in black and, thus, its emissivity coefficient was exactly known. Since the heat diffusivity of this solid surface is $\alpha_s = 64\ \mathrm{m}^2/\mathrm{s}$, diffusion time within it was approximately $h_s^2/\alpha_s \approx 10^{-6}$ s, signifying that the steel foil almost instantaneously reflected the temperature at the liquid bottom. However, the upper mirror was inevitably implemented to detect the droplet deposition time and spreading/receding dynamics, enabling us to synchronize it with the signals received from the lower mirror. Furthermore, it took some time for any thermal signature to be advected from the methanol/oil interface into the oil and ultimately to the bottom. From the upper mirror signals, we were able to precisely detect when the methanol droplet reached the oil surface. A comparison between the signals recorded from the upper and lower mirrors is provided in Fig. 2.

However, the first detectable signal on the lower mirror appeared after some delay Δt, which is the time for temperature changes to travel along the oil layer. To estimate this delay we calculated the L^2-norm difference of the temperature field between consecutive frames after droplet deposition. Temperature field before drop deposition was considered as the base condition. Figure 3 provides the L^2-norm variations starting from droplet deposition time $t = 0$. The increase in L^2-norm difference indicates the emergence of thermal effects at the bottom of the oil. At $t = 2.9$ s, the L^2 norm was twice its average initial value. Therefore, $\Delta t = 2.9$ s was considered as the delay time between the first and second mirrors. Aside from this experimental observation, a more detailed investigation of the delay time was necessary to determine whether it originated in conduction heat transfer or convection. In Appendix, a theoretical discussion is provided which clearly demonstrates that, for a pure conduction mechanism, the delayed time would be at least ten times bigger. Based on this theoretical analysis we came to the conclusion that convection is the primary mechanism for heat transfer.

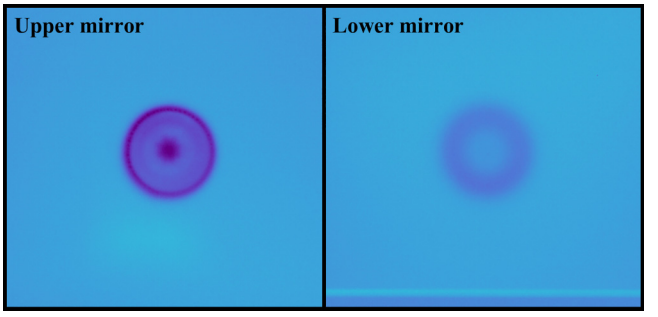

FIG. 2. Comparison of recorded signals from upper and lower mirrors. The upper mirror provided a qualitative description of the temperature field, while data obtained from the lower mirror were quantitatively accurate.

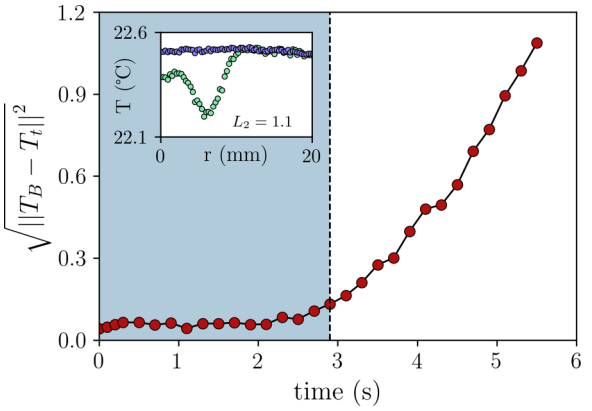

FIG. 3. L^2-norm difference of temperature field calculated from temperature field before droplet deposition. At $t = 2.9$ s, the L^2 norm is doubled compared to its early time value. The subset plot shows an example of temperature difference between the base condition and temperature field at $t = 5.5$ s.

B. Optical measurement of the deposited evaporating drop volume

Visualization photographs were further processed by the Beer-Lambert-Bouguer (BLB) law to estimate the droplet thickness at different stages of development. When light interacts with a liquid (herein, methanol), its intensity decays along its propagation from absorption and scattering. As methanol was dyed in our experiment, its absorption was increased and hence measurable. The BLB law relates the light intensity reduction to the traveling path within the medium. According to the BLB law, the radiant intensity of a beam after traveling a distance of h through a medium is

$$I(h) = I_0 e^{-\beta h}, \tag{2}$$

where I_0 is the incident intensity and β is the attenuation or extinction coefficient. The calibration of the attenuation coefficient β for dyed methanol permits the use of the BLB law to evaluate the local thickness of the droplet. To do so, we deposited different dyed methanol volumes using the microfluidic pump ranging from 6 to 12 μL. Using the first image of the droplet after deposition, we could evaluate the intensity distribution, $I(r, \theta)$, from RGB values of the image. Images taken from the oil surface before the droplet release provided the constant intensity, $I_0(r, \theta) = I_0$. Rearranging Eq. (2) leads to

$$h(r, \theta) = -\frac{1}{\beta} \ln\left(\frac{I(r, \theta)}{I_0}\right). \tag{3}$$

Up to here, both $h(r, \theta)$ and β are unknown. Due to the symmetry of the droplet both thickness and intensity very weakly depend on the azimuth, θ, so that an average intensity over θ can be computed. Since the exact volume of the deposited volume is known and also because we use the first image where evaporated mass is negligible, we can complete the calibration from computing the droplet volume,

$$V = 2\pi \int_0^R h(r) r \, dr, \tag{4}$$

replacing $h(r)$ from Eq. (3), which leads to

$$V = -\frac{2\pi}{\beta} \int_0^R \ln\left(\frac{I(r)}{I_0}\right) r \, dr. \tag{5}$$

For a given volume, there is only one single value of β satisfying Eq. (5). Obtaining β for a set of experiments with different deposited volumes permits one to find an averaged value for the

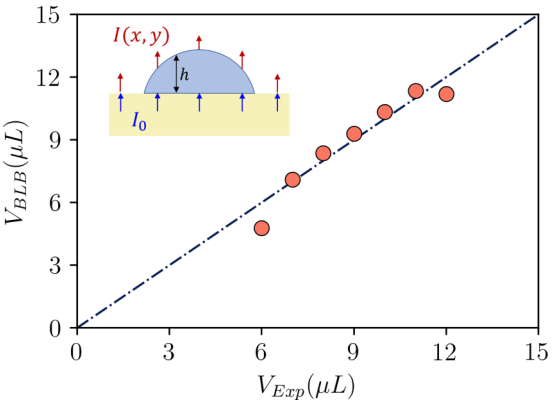

FIG. 4. Calibration of attenuation coefficient, β, in Beer-Lambert-Bouguer law.

attenuation coefficient. For this unique β, the volumes predicted by Eq. (5) are compared with the experiments in Fig. 4. Given Fig. 4, a good agreement is found between prediction and prescribed volume (central diagonal depicts perfect agreement). This confirms the validity of this droplet thickness' evaluation method. Results of volume measurements are discussed in Sec. V.

III. EXPERIMENTAL OBSERVATIONS

As soon as the methanol drop reaches the oil surface, a series of instabilities happen consecutively and in very short duration. A temporal sequence of the flow development is illustrated in Fig. 5(a). In this figure, a 30 µL droplet was deposited over an 8 mm thick oil layer. Methanol drop spontaneously spreads over the oil surface because of the small interfacial tension between the two liquids and the positive spreading coefficient, $S = \gamma_o - \gamma_d - \gamma_{od} > 0$. Segments with red and blue arrows, respectively, indicate spreading ($t < 12.9$ s) and receding ($t > 12.9$ s) phases of the

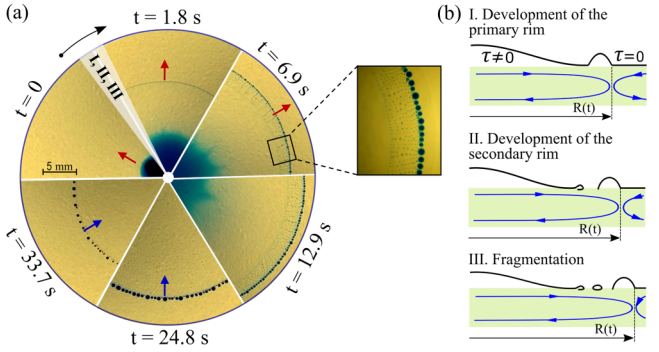

FIG. 5. Dynamics of a methanol droplet deposited on an olive-oil layer. (a) Top-view droplet development over oil layer. When the outer rim reaches a maximum extent from solutal Marangoni tangential stress it starts receding from the thermal one. Capillary length has been estimated to be $\ell_c = 4$ mm. (b) Transverse schematic representation of the rim fragmentation steps arising within the short-time period depicted in (a) as I, II, and III. (I) The rim is first detached by Marangoni-stress arising between the free-stress region $\tau = 0$ on the right to the nonzero one $\tau \neq 0$ on the left. This stress also induces a reverse backflow inside the oil depicted with blue arrows. (II) After detachment, a secondary rim develops and progressively wrinkles circumferentially. (III) After a finite time, the secondary rim destabilizes, leading to the formation of smaller daughter drops hereafter continuously shed from the secondary rim.

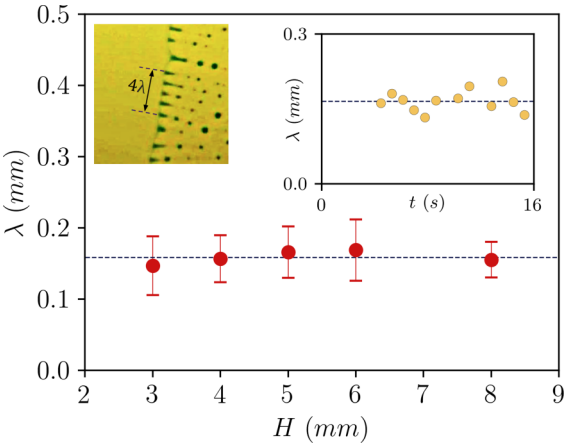

FIG. 6. Wavelength measurements of the fingering instability for different depths of oil, H.

flow development. Ahead of the bulk flow, a shear-free precursor film propagates very fast over the whole oil surface [24,25]. This far propagating precursor region being shear free ($\tau = 0$) needs to match with the nonzero stress ($\tau \neq 0$) zone within the droplet, leading to a strongly localized solutal Marangoni stress resulting from positive spreading coefficient, S, and leading to the formation of a rim at the interface of the two regions [step I, Fig. 5(b)]. This primary rim forms shortly after the drop deposition and thickens as it moves outward until detaching from the main droplet by capillary rupture [step II, Fig. 5(b)]. Resulting from detachment, a thinner secondary rim develops at the periphery of the main droplet. The circumferential shape of this secondary rim, at early stages being smooth, soon enough destabilizes and adopts a wavy shape. Along this unstable rim, liquid accumulates at the crest points from surface tension and circumferentially develops a large number of ligaments which then break as also studied in [26,27]. The process thus repeats itself, leading to small droplet detachment, fed by the rim resulting in a train of small, almost equal size, droplets [step III, Fig. 5(b)]. The zoom region in Fig. 5(a) illustrates the trains of these droplets detaching from the secondary rim and progressively merging outward within large pearlized drops.

As discussed in the Introduction, this bursting of the volatile droplet into a large number of small droplets was first observed by Keiser *et al.* [20]. Uncertain about the mechanism responsible for the bursting, they attributed it to some moving contact line instabilities. In later studies carried out by Hasegawa and Manzaki [22] and Seyfert and Marin [21], the origin of this instability was disregarded. Here we investigate if the Rayleigh-Plateau instability acts on the secondary rim and triggers its fragmentation. Rayleigh-Plateau instability can be recognized by a universal characteristic ratio known as Rayleigh ratio, which is stated as [26]

$$c = \frac{\lambda}{W}, \tag{6}$$

where λ is the instability wavelength and W is the rim width. If this ratio is found to be around 2.4, the instability results from a Rayleigh-Plateau mechanism. Two sets of experiments for measuring the wavelength and the width have been performed. In the first set, a camera has been equipped with an AF Micro Nikkor 200 mm $f/4D$ lens that remarkably magnified the instability features along the interfacial front. An example of the magnified visualizations is provided in the subset of Fig. 6. As seen, the fingering instabilities were captured in great detail, making wavelength measurements reliable. These measurements are reported in Fig. 6 for various oil depths ranging from $H = 3$ mm to $H = 8$ mm. It reveals that the observed wavelength very weakly varies with H, with a nearly constant value of $\lambda \approx 0.16$ mm. Measurements of rim width, W, are much more delicate, since it is very thin and hardly identifiable with direct visualization. To address the issue, an interferometric

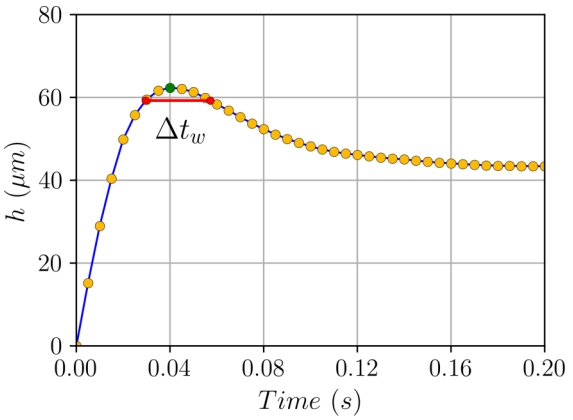

FIG. 7. Typical measurement of rim width using an interferometric confocal sensor.

method which can perform fast and accurate scans of transparent fluid layers has been chosen. A CHRocodile 2S sensor unit equipped with a 3 mm chromatic confocal has been used. This material can perform measurements with a frequency up to 50 kHz and with a vertical resolution of 100 nm. A typical measurement of the rim is provided in Fig. 7. The sensor tip is fixed at 5 mm away from the droplet deposit center so as to ensure the rim capture. We assume that the rim shape follows a parabolic shape nearby its maximum, so that a quadratic relation is supposed $h(x) = h_0[1 - x^2/(2R_r h_0)]$, where h_0 is the maximum height of the rim, so that the second derivative $h(x)$ is precisely the curvature equal to the inverse of the curvature radius $1/R_r$. The curvature radius of the rim is considered to be R_r; then the width of the rim is obtained from condition $h(\pm W/2) = 0$, i.e.,

$$W = 2\sqrt{2R_r h_0}, \tag{7}$$

where $R_r = U\,\Delta t_w$. From interferometric measurements, $\Delta t_w \simeq 0.027$ s (shown with a red line in Fig. 7), and typical velocity of the spreading is around 10 mm/s. Having R_r and replacing it back into Eq. (7) with $h_0 \simeq 2.8$ μm, we get to $W = 0.078$ mm. Using the measured value of wavelength, the universal characteristic ratio is obtained to be 2.03, which is close to the criterion for the Rayleigh-Plateau instability. Therefore, the fingering instability observed around the droplet edge is most probably resulting from the Rayleigh-Plateau instability mechanism. As complex as it may be, the spreading dynamics was not much of a surprise as previously reported in similar configurations [20]. Nevertheless, the reversed flow associated with the drop recession observed after time t_{rc} reported in Fig. 5, as well as the subsequent shrinkage due to evaporation leading to final disappearance, was quite unexpected. With the methanol evaporation, solutal Marangoni forces weakened and were unable to spread the liquid further after a certain time. Concurrently, the cooling resulting from the methanol phase change induced a low-temperature region where strong evaporation fluxes arose. This interpretation is supported by the results obtained from the infrared thermography experiments.

The main results from temperature measurements are reported in Fig. 8. These measurements are obtained from the lower mirror and synchronize with the signal recorded from the top mirror. As explained in Sec. II, drop radius $R(t')$ at delayed time $t' = t + \Delta t$ can be detected from the upper mirror. Identification of $R(t')$ was critically important as the temperature gradients near the edge of the spreading drop are of the most interest. Also, it was shown in Sec. II that the time delay, Δt, is provided by a convection dominated (dimensionless Péclet number and pure diffusion computation provided in Table II) transfer associated with the Stokes-flow induced by the top drop Marangoni tangential shear down into the oil layer. The general pattern of this flow is depicted in Fig. 5(b) as blue arrows and also discussed in the Supplemental Material of [20]. To provide a more detailed description, we made a quantitative estimation of the convection time and compared it with the

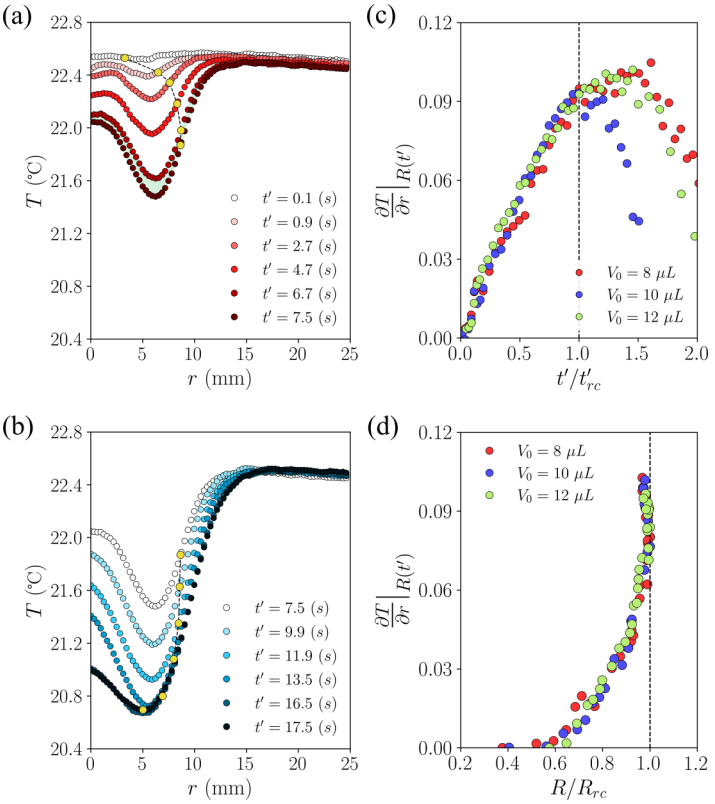

FIG. 8. (a) Radial distribution of temperature during the spreading stage and (b) during the receding stage. (c) Radial gradient of temperature measured at the front, $R(t')$, plotted against t'/t'_{rc}. (d) Radial gradient of the temperature measured at the front plotted versus R/R_{rc}.

experimental value. Convection time, t_{cv}, is defined as

$$t_{cv} = \frac{H}{U_0}, \tag{8}$$

where H is the oil thickness and U_0 is the typical velocity of the oil layer backflow, which will be evaluated from the tangential-stress continuity condition

$$U_o = \frac{\mu_d}{\mu_o}\frac{H}{h}U_d, \tag{9}$$

wherein U_d is the typical deposited drop velocity and h_0 is the typical drop height. Using the experimental values $\mu_d/\mu_o \approx 6.5 \times 10^{-3}$, $H/h_0 \approx 20$, and $U_d \approx 10^{-2}$ m/s, it is found that the convection time for the oil thickness of $H = 3.8$ mm used in the infrared thermography experiments gives a delay time of $\Delta t \approx 2.9$ s. This Δt is completely consistent with the one obtained from experimental observations.

Radial variations of temperature are given in Figs. 8(a) and 8(b), respectively, during the spreading and receding stages. In both plots, results are presented at different times with the corresponding front positions $R(t' = t + \Delta t)$ indicated by yellow symbols. For a better comparison, temperature profile at $t' = 7.5$ s is provided in both plots. Moving away from the droplet center, temperature constantly decreases, reaches a minimum, and then increases gradually until settling back to the room temperature. As seen, the minimum temperature happens just before the drop edge.

Actually, not only the largest radial temperature gradients are found nearby the drop edge during the spreading stage [Fig. 8(a)] but also in the receding one [Fig. 8(b)]. Using the synchronization between the upper and lower image recordings, we can also reconstruct the Lagrangian temperature gradient of the moving droplet edge, as represented in Figs. 8(c) and 8(d). It can be observed that this temperature gradient increases during the spreading phase (for $t < t_{rc}$), to reach its maximum nearby the receding time $t = t_{rc}$ [Fig. 8(c)]. A similar observation can be raised for the temperature gradient at the drop edge being maximal at the receding maximal radius $R = R_{rc}$ [Fig. 8(d)]. Moreover, comparing temperature gradient results for different volumes ranging from 8 μL to 12 μL also suggests that the gradient is independent of droplet volume. Consequently, the nonuniform evaporation of the droplet from the apex to the contact line created both temperature and surface tension gradients. These gradients built an inward thermal Marangoni stress responsible for the receding reported in Fig. 5(a).

In the following, we focus on a quantitative understanding of the physics behind the spreading/recession dynamics.

IV. THEORETICAL ANALYSIS

This section considers some aspects of the reported experimental observations, but does not have the aim to provide an extensive theoretical analysis of the considered spreading problem. In fact such an aim is quite involved and deserves an extended analysis *per se*. Here we focus on the following aspects: early-time spreading dynamic, evaporation rate/volume decaying rate, and receding time. We then consider first the early-time behavior of the deposited drop, ignoring thermal Marangoni effects induced by the volatile droplet evaporation. This approximation is built upon the isothermal initial condition between the two liquids. This has been accurately confirmed by direct thermography experimental measurements and therefore it is a sensible assumption.

Thin-film lubrication dynamics (dimensionless numbers given in Table II that support a lubricated noninertial flow) for the axisymmetric spreading drop height $h(r, t)$ in cylindrical coordinates centered at the drop deposit center reads as follows:

$$\frac{\partial h}{\partial t} + \frac{1}{r}\frac{\partial}{\partial r}\{rQ\} + \frac{j}{\rho_d} = 0, \tag{10}$$

where Q is the radial fluid flux defined as the integral of the radial velocity u_r, $Q = \int_0^h u_r(z)dz$, j is the evaporation mass flux, and ρ_d the deposit drop density. The Stokes lubrication equations in r direction are solved applying a free-stress condition at $z = h$ and assuming negligible velocity at the oil-methanol interface $z = 0$ to find the flux Q in (10). This assumption is, in fact, based upon an asymptotic approximation of tangential shear-stress continuity since the velocity ratio between the deposit methanol to the oil is $O(\mu_d/\mu_o) \ll 1$ small. The radial velocity field within the deposited droplet can then be found [up to $O(\mu_d/\mu_o)$ corrections]:

$$u_r(r, z) = \frac{1}{\mu_d}\frac{\partial p}{\partial r}\left(\frac{z^2}{2} - zh\right) + \frac{1}{\mu_d}\frac{\partial \gamma}{\partial r}z, \tag{11}$$

wherein p is the z-invariant pressure within the spreading deposited droplet, μ_d its dynamic viscosity, and γ the (spatially varying) deposited droplet/air surface tension. Using Eq. (11) to find the radial fluid flux Q substituted in Eq. (10) leads to

$$\frac{\partial h}{\partial t} + \frac{1}{r}\frac{\partial}{\partial r}\left\{-\frac{r}{3\mu_d}\frac{\partial p}{\partial r}h^3 + \frac{r}{2\mu_d}\frac{\partial \gamma}{\partial r}h^2\right\} + \frac{j}{\rho_d} = 0. \tag{12}$$

Equation (12) is the nonlinear evolution equation of the deposit droplet taking into account the thermal effects, embedded into the surface tension gradient and the evaporation mass flux j. Realizing that the pressure provided by normal-stress continuity at the deposited drop free surface is given by the (linearized) Laplace law $p = \gamma \Delta_r h$ associated with the radial component of the cylindrical

Laplacian, it is possible to find that the hydrodynamic pressure gradient term in Eq. (12) is always negligible compared to the Marangoni one associated with the surface tension gradient. Since radial variations are associated with the capillary length ℓ_c, with h being related to some reference thickness h_0 (with lubrication small parameter condition $h_0/\ell_c \ll 1$), we can scale pressure and Marangoni terms as

$$h^3 \frac{\partial p}{\partial r} \sim h_0^3 \frac{1}{\ell_c} \frac{\gamma_d h_0}{\ell_c^2} \sim \left(\frac{h_0}{\ell_c}\right)^2 \frac{\gamma_d h_0^2}{\ell_c}, \tag{13}$$

$$h^2 \frac{\partial \gamma}{\partial r} \sim \frac{\gamma_d h_0^2}{\ell_c}, \tag{14}$$

implying that the pressure gradient is $(h_0/\ell_c)^2$ smaller than the Marangoni one, with the latter being the leading order term to consider. Negligible evaporation at early time and consequently insignificant thermal effects at the early stage of methanol development (this assumption is confirmed by the volume measurements provided in the following section) leads to a simplification of (12) as

$$\frac{\partial h}{\partial t} + \frac{1}{r}\frac{\partial}{\partial r}\left(\frac{r}{2\mu_d}\frac{\partial \gamma}{\partial r} h^2\right) \approx 0. \tag{15}$$

Now considering that the solutal Marangoni spreading is convectively dominated and thus Lagrangian invariant, one gets

$$\frac{D\gamma}{Dt} = \frac{\partial \gamma}{\partial t} + u_r \frac{\partial \gamma}{\partial r} = 0. \tag{16}$$

It is then possible to derive a similarity solution for the early-time spreading of the methanol droplet. More precisely, from defining the spreading typical time as given by the capillary-viscous time t_{cv} built upon the capillary length ℓ_c and the kinematic viscosity of the deposited drop, i.e., $t_{cv} = \ell_c^2/\nu_d$ (as used in many various other studies [28]), an approximate solution for dimensionless time $t/t_{cv} \ll 1$ is searched for. For methanol, at room temperature $T = 293.15$ K, one finds $t_{cv} = 4.2$ s, which is precisely of the order of the receding time t_{rc} which is found in the range $t_{rc} \sim 3$–9 s for deposited drop volume V_0 in the range 8–12 µl.

We then seek a self-similar solution $h(r,t) = t^{-\alpha} f(\zeta)$ with rescaled variable $\zeta = r/t^{\beta}$ in (15) (as also suggested by recent numerical computations of lubrication's analysis of a close problem [29]), where the surface tension gradient term $\partial\gamma/\partial r$ needs to be evaluated. Chain rule thus provides

$$\frac{\partial \gamma}{\partial r} = \frac{\partial \zeta}{\partial r}\frac{\partial \gamma}{\partial \zeta} + \frac{\partial t}{\partial r}\frac{\partial \gamma}{\partial t} = \frac{1}{t^{\beta}}\left(\frac{\partial \gamma}{\partial \zeta} + \frac{t}{\beta \zeta}\frac{\partial \gamma}{\partial t}\right). \tag{17}$$

Furthermore, considering (16) and the Marangoni-dominated velocity field (12) leads to $\partial\gamma/\partial t \approx -\frac{h}{\mu_d}(\partial\gamma/\partial r)^2$. This leads to evaluating the last right-hand side (RHS) term of Eq. (17) to scale as $(t/\beta)(h_0/\ell_c)(\gamma_d/\mu_d\ell_c)(\gamma_d/\zeta)$ to be compared with $\partial\gamma/\partial\zeta \sim \gamma_d/\zeta$. Defining the capillary number as $\mathrm{Ca} = \mu_d\ell_c/\gamma_d t_{cv}$, one finds that the last term of Eq. (17) is small compared with $\partial\gamma/\partial\zeta$ with the early-time assumption $(h_0/\ell_c)(t/t_{cv})/\mathrm{Ca} \ll 1$. Then, within this early-time approximation, $\partial\gamma/\partial r \approx \partial\gamma/\partial\zeta/t^{\beta}$, and Eq. (15) satisfies self-similarity, i.e., becomes time independent, if $2\beta + \alpha = 1$. To complete the system of equations, we use the assumption of thin droplets to approximate the deposited droplet of radius $R(t)$ and initial volume V_0 with $V_0 \sim R(t)^2 h$. Using again an early-time assumption for which the volume is considered constant, seeking self-similar $R(t)$ and $h(r,t)$ in the constant volume constraint, one gets $\alpha = 2\beta$. This finally provides $\alpha = 1/2$, $\beta = 1/4$, so that, at early time,

$$\frac{R(t)\sqrt{h_0}}{\sqrt{V_0}} \sim \left(\frac{t}{t_{cv}}\right)^{1/4}. \tag{18}$$

In order to find an estimation for the recession time t_{rc}, we now consider the evaporation rate. Assuming a thin droplet with a diffusion-limited evaporation, local flux of evaporation is approximated

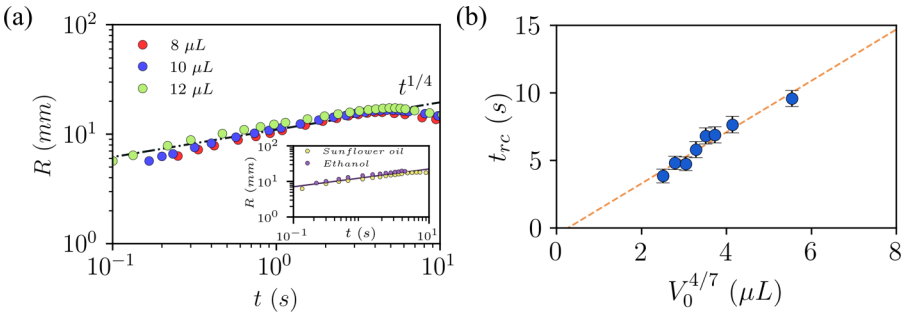

FIG. 9. (a) Log-log plot of the spreading drop radius $R(t)$ versus time measured for different initial volumes V_0. The similarity solution, $R(t) \sim t^{1/4}$, is provided with dotted lines. (b) Recession time, t_{rc}, plotted versus $V_0^{4/7}$ confirming scaling of Eq. (22).

as [28,30]

$$j(r,t) = \frac{j_0}{R(t)\sqrt{[1-(r/R)]^2}}, \tag{19}$$

where j_0 is a constant dependent on the liquid properties and $R(t)$ is again the droplet radius. Integrating along r in cylindrical coordinates, the total evaporation flux is proportional to the radius, i.e., $J(t) = \int_0^R j(r,t) r\, dr = 2\pi j_0 R(t)$. The time variation of the droplet volume then reads

$$\frac{dV}{dt} = -\frac{A_d}{\rho_d} J(t), \tag{20}$$

wherein A_d is the surface area of the droplet. Through the assumption of spherical cap one gets $A_d = \pi[R^2(t) + h^2(0,t)]$ and, from $R^2 \gg h^2$, $A_d \approx \pi R^2(t)$. Using the scaling $R(t) \sim t^{1/4}$ a relation for droplet volume as a function of time is suggested,

$$V(t) - V_0 \approx -\left(\frac{2\pi^2 j_0}{\rho_d}\right) t^{7/4}. \tag{21}$$

Based on experimental observations, the recession happens nearly around the complete evaporation of the droplet. Therefore, solving Eq. (21) from $t = 0$ where $V = V_0$ to $t = t_{rc}$ with $V(t_{rc}) \simeq 0$, one gets

$$t_{rc} \sim V_0^{4/7}. \tag{22}$$

It is worth mentioning that this recession time has been derived from the assumption of complete evaporation at recession time, based upon experimental observations (from 90 to 95% as provided in Fig. 10). Finally, it is also interesting to pinpoint that, nearby the receding time, the final evaporation behavior differs from Eq. (22) since, nearby this point, the drop radius is almost immobile, so that $R(t) \approx R_{rc}$. In this case the RHS of Eq. (20) scales as $R^3(t) \sim R_{rc}^3$ and is thus almost constant leading to both a linear time variation of the film height $h(t) \sim t$ and volume $V(t) \sim R_{rc}^2 h(t) \sim t$.

V. COMPARISON BETWEEN THEORETICAL MODELs AND EXPERIMENTS

Figure 9(a) displays the time variation of the deposited drop radius $R(t)$ for initial volumes of 8, 10, and 12 μL, and convincingly compares it to the early-time similarity prediction $R(t) \sim t^{1/4}$. Given that the capillary-viscous time is $t_{cv} = 4.2$ s, deviations from this scaling behavior can be observed after a few seconds have elapsed. As seen, experimental measurements follow the theoretical power-law trend up to nearby the receding time, which justifies the implementation of the self-similar solution into Eq. (21). To investigate further the universality of this self-similar solution,

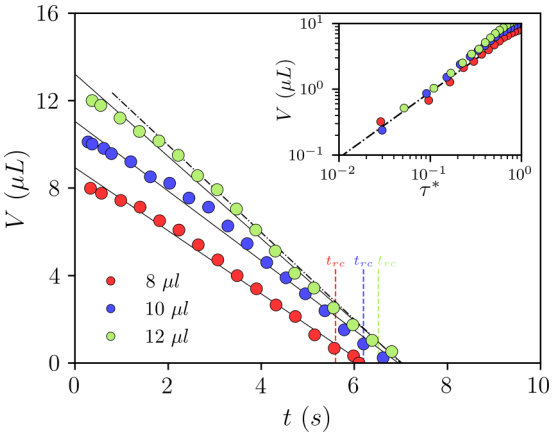

FIG. 10. Time variation of the deposited droplet volume for three distinct deposited initial volumes $V_0 = 8, 10, 12\ \mu L$. The solid line represents the early-time approximated model (22) without any adjustable parameters. Dotted lines give late-time drop volume prediction $V \sim \tau^*$ nearby receding time t_{rc}. The inset displays these volume variations in log-log plot for a better identification of this late-time linear variation.

supplementary experiments have been carried out with different fluid couples as illustrated in the inset of Fig. 9(a). As in previous contributions using organic oils [20–22], sunflower oil has been used instead of olive oil for the deep layer fluid with a methanol deposited drop and, furthermore, ethanol deposited drop over olive oil has also been tested. In both cases the experimental results are very consistent with the power-law prediction (18). It is also worth mentioning that silicone oil (350 cst) deep layer coupled with methanol deposited droplet has also been tested. In this case, as expected from the resulting spreading parameter S, the methanol droplet did not spread on the silicone oil. In fact, due to the low surface tension of silicone oil ($\gamma_s \simeq 20$–25 mN/m), S is negative in this configuration so that the methanol droplet remains still on the oil surface and gently evaporated as a sessile drop.

Examining the theoretical model suggested by Eq. (22), recession time was measured for a wider range of initial deposited volumes of methanol. Considering the scaling proposed by the model, recession time measurements were plotted against $V_0^{4/7}$. The dashed line represents a linear fit of the experimental data, confirming the linear relationship between t_{rc} and $V_0^{4/7}$ and thus validating the theoretical analysis that was performed.

As discussed in Sec. III, Beer-Lambert-Bouguer law was used to obtain a detailed map of droplet thickness and consequently volume. Figure 10 illustrates the temporal variations of droplet volume are plotted for initial volumes of 8, 10, and 12 μL. Corresponding recession times, t_{rc}, are also reported in this figure. It is noticeable that receding occurs when the droplet has almost completely evaporated. This confirms the assumption made in deriving Eq. (22) that $V(t_{rc}) \simeq 0$. Depicted by solid lines, the droplet volume variations predicted in (21) (compared without adjusted parameters) quite surprisingly closely follows the experimental observation very near to the receding time. Finally, the late-time dynamics of the volume shrinkage is also compared with measurements in the figure inset. In this log-log plot, τ^* is defined as $(t_{rc} - t)/t_{rc}$ and accordingly the linear trend with volume nicely supports the ouput of the volume theory in the previous section.

VI. CONCLUSIONS

Simultaneous effects of interfacial tensions and nonuniform evaporation of a droplet can give rise to highly complex flows and surprising patterns of spreading dynamics. In the present study,

the dynamics of a methanol droplet deposited on an immiscible layer of oil, with positive spreading parameter S, has been studied both experimentally and theoretically.

Upon releasing, the methanol droplet first spreads due to the solutal Marangoni stress. Even though spreading was expected, the succeeding reverse flow and droplet recession was not. To understand the mechanism underneath this secondary recession, a specific experimental setup has been designed using infrared thermography analysis. The resulting measurements revealed that preferential cooling evaporation at the drop edge induces a temperature gradient reaching a maximum at the recession time, consequently creating an inward thermal Marangoni stress. Losing most of its volume by evaporation, the thermal Marangoni overcame the diminishing solutal one, finally causing recession. Moreover, using Beer-Lambert-Bouguer law for processing flow visualizations, the temporal variations of droplet volume have been tracked. In addition to the experimental investigations, a theoretical model has been developed using lubrication approximation. A self-similar solution for the early time spreading phase, for which the droplet radius follows a power-law behavior $R \sim t^{1/4}$, has been found. This power-law prediction matches very well with experimental results. Based on this solution, a second prediction for the deposited drop volume variation has been derived taking into account the evaporation rate in the framework of a diffusion-limited evaporation model for droplet shape semispherical cap approximation. The resulting predictions also satisfactorily compare with experiments. A complete theoretical understanding of the considered problem is nevertheless far from complete and deserves extended attention for a more comprehensive understanding of the reported thermal Marangoni building temperature at the spreading drop's edge.

ACKNOWLEDGMENTS

A.J. acknowledges American Chemical Society Grant No. PRF 61071-ND9 funding. Additionally, we would like to thank S. Cazin from IMFT for suggesting the configuration of thermal measurement setup and for his assistance in using the infrared camera. We also extend our thanks to C. Korbuly for his help in the design and machining of the experiments.

APPENDIX: THERMAL DIFFUSION CROSS EVALUATION

As discussed in Sec. II, a time delay of 2.9 s was experimentally observed between temperature signals of upper and lower mirror. This delay was attributed to the time required for the transfer of temperature effects from the upper surface to the lower surface of the oil. In this Appendix, we conducted a theoretical evaluation to determine if conduction is the primary mechanism of heat transfer or not. We begin by considering pure conduction heat transfer in the oil layer in order to estimate the time delay arising without advection. Heat-transfer energy conservation within a thin layer of thickness H reads

$$k\left[\frac{\partial^2 T}{\partial x^2}+\frac{\partial^2 T}{\partial y^2}+\frac{\partial^2 T}{\partial z^2}\right]=\rho c_p\frac{\partial T}{\partial t}. \tag{A1}$$

Nondimensionalizing this equation by defining $\phi = (T - T_0)/T_0$, where T_0 is the room temperature, while also using

$$x = LX,$$
$$y = LY,$$
$$z = HZ,$$
$$t = t_0\tau,$$

where H is the thickness of the oil bath, t_0 the typical diffusive time evaluated from $\rho c_p H^2/k$, and L the characteristic length such that $\epsilon \equiv H/L \ll 1$, leads to

$$\left[\epsilon^2\left(\frac{\partial^2\phi}{\partial X^2}+\frac{\partial^2\phi}{\partial Y^2}\right)+\frac{\partial^2\phi}{\partial Z^2}\right]=\frac{\partial\phi}{\partial\tau}, \tag{A2}$$

where $\alpha = k/\rho c_p$ is the thermal diffusivity. We then seek an asymptotic approximation of (A.2), which at leading order reduces to

$$\frac{\partial^2\phi}{\partial Z^2}=\frac{\partial\phi}{\partial\tau}. \tag{A3}$$

A separation of variable for ϕ solution leads to

$$(X, Y, Z, \tau) = \psi(X, Y)\Theta(Z, \tau). \tag{A4}$$

Using (A.4) in (A.3) leads to

$$\frac{\partial^2\Theta}{\partial Z^2}=\frac{\partial\Theta}{\partial\tau}. \tag{A5}$$

The boundary conditions for the temperature applied from methanol into the oil layer at $Z = 0$ are then split into a spatially varying part taken care of by $\psi(X, Y)$ and a homogeneous part associated with $\Theta(Z, t)$, so that the boundary conditions associated with $\Theta(Z, t)$ are

$$\begin{aligned}\frac{\partial\Theta}{\partial Z}&=\mathrm{Bi}\Theta, \quad Z=-1,\\ \Theta&=1, \quad Z=0,\end{aligned} \tag{A6}$$

where the boundary condition at $Z = -1$ comes from the free convection heat transfer where Bi stands for the Biot number as $\mathrm{Bi} = h_{cv}H/k$, with h_{cv} as the convection heat transfer coefficient. The initial condition is homogeneous, i.e., $\Theta(Z, \tau = 0) = 0$. Equation (A.6) is a nonhomogeneous boundary value problem that can be transformed into a homogeneous one following decomposition

$$\Theta(Z, \tau) = \widetilde{\Theta}(Z, \tau) + \Theta'(Z), \tag{A7}$$

with $\acute{\Theta}(Z = 0) = 1$ and $\partial_Z\Theta' = \mathrm{Bi}\Theta'$ at $Z = -1$. Solving for Θ', we find

$$\Theta'(Z) = \frac{1+\mathrm{Bi}(Z+1)}{1+\mathrm{Bi}}. \tag{A8}$$

Then the equation and boundary conditions for $\widetilde{\Theta}$ are now homogeneous:

$$\frac{\partial^2\widetilde{\Theta}}{\partial Z^2}=\frac{\partial\widetilde{\Theta}}{\partial\tau}, \tag{A9}$$

$$\begin{aligned}\frac{\partial\widetilde{\Theta}}{\partial Z}&=\mathrm{Bi}\widetilde{\Theta}, \quad Z=-1,\\ \widetilde{\Theta}&=0, \quad Z=0.\end{aligned}$$

We again seek for a separation of variables solution for $\widetilde{\Theta}$ upon a discrete set of modes θ_n from the infinite series

$$\widetilde{\Theta}(Z, \tau) = \sum_{n=1}^{\infty} A_n\theta_n e^{-\lambda_n^2\tau}, \tag{A10}$$

where modes θ_n are decomposed into the discrete eigenfunctions of (A.9)

$$\theta_n = \sin(\lambda_n Z) \tag{A11}$$

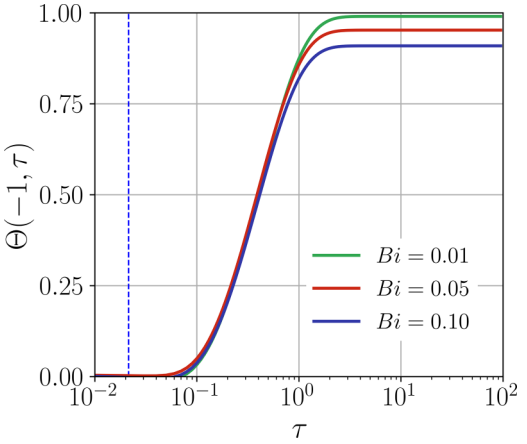

FIG. 11. Variation of Θ at $Z = -1$ for Biot numbers of 0.01, 0.05, and 0.1.

for which the associated eigenvalue λ_n permits one to fulfill the homogeneous boundary conditions from the (transcendental) spectral problem

$$\lambda_n = -\mathrm{Bi}\,\tan(\lambda_n). \tag{A12}$$

The amplitude of decomposition (A.10) is found from projection into modes θ_n,

$$A_n = \frac{\langle \Theta'(Z), \theta_n \rangle}{\langle \theta_n, \theta_n \rangle} = -4\frac{\mathrm{Bi}\lambda_n \sin(\lambda_n) + \lambda_n^2 \cos(\lambda) - \lambda_n^2(1+\mathrm{Bi})}{(1+\mathrm{Bi})\lambda_n^2[2\lambda_n - \sin(2\lambda_n)]}. \tag{A13}$$

From (A.7) we finally have

$$\Theta(Z,\tau) = \frac{1+\mathrm{Bi}(Z+1)}{1+\mathrm{Bi}} + \sum_{n=1}^{\infty} A_n[\sin(\lambda_n Z)]e^{-\lambda_n^2\tau} \tag{A14}$$

and at $Z = -1$

$$\Theta(-1,\tau) = \frac{1}{1+\mathrm{Bi}} - \sum_{n=1}^{\infty} A_n \sin(\lambda_n) e^{-\lambda_n^2\tau}. \tag{A15}$$

The value of $\Theta(-1,\tau)$ matters most since its time variations indicate when the temperature of the upper surface $\Theta(0,\tau) = 1$ reaches the lower surface through conductive heat transfer. $\Theta(-1,\tau)$ for several Biot numbers is given in Fig. 11. As seen, τ must be higher than 20 for $\Theta(Z=-1)$ to approach 1.0. From experiments, we had a translational time of 2.9 s; if divided by the reference time we can find the corresponding value of $\Theta(-1, \tau = 2.9/t_0)$. As plotted in Fig. 11 with a blue dashed line, the corresponding $\Theta(-1,\tau)$ is nearly zero for $\tau = 2.9/t_0$, which clearly indicates that conduction cannot be the heat transfer mechanism from the upper surface to the lower one.

[1] V. Bergeron, D. Bonn, J. Y. Martin, and L. Vovelle, Controlling droplet deposition with polymer additives, Nature (London) **405**, 772 (2000).

[2] S. Shiri, S. Sinha, D. A. Baumgartner, and N. J. Cira, Thermal Marangoni Flow Impacts the Shape of Single Component Volatile Droplets on Thin, Completely Wetting Substrates, Phys. Rev. Lett. **127**, 024502 (2021).

[3] J.-L. Zhu, W.-Y. Shi, and L. Feng, Bénard-marangoni instability in sessile droplet evaporating at constant contact angle mode on heated substrate, Int. J. Heat Mass Transfer **134**, 784 (2019).
[4] T. Pham and S. Kumar, Drying of droplets of colloidal suspensions on rough substrates, Langmuir **33**, 10061 (2017).
[5] A. Amini and G. M. Homsy, Evaporation of liquid droplets on solid substrates. II. Periodic substrates with moving contact lines, Phys. Rev. Fluids **2**, 043604 (2017).
[6] J. F. Hernández-Sánchez, A. Eddi, and J. H. Snoeijer, Marangoni spreading due to a localized alcohol supply on a thin water film, Phys. Fluids **27**, 032003 (2015).
[7] D. K. N. Sinz, M. Hanyak, and A. A. Darhuber, Immiscible surfactant droplets on thin liquid films: Spreading dynamics, subphase expulsion and oscillatory instabilities, J. Colloid Interface Sci. **364**, 519 (2011).
[8] S. Tsuchitani, T. Fukutake, D. Mukai, H. Miki, and K. Kikuchi, Unstable spreading of ionic liquids on an aqueous substrate, Langmuir **33**, 11040 (2017).
[9] F. Wodlei, J. Sebilleau, J. Magnaudet, and V. Pimienta, Marangoni-driven flower-like patterning of an evaporating drop spreading on a liquid substrate, Nat. Commun. **9**, 820 (2018).
[10] X. Ma, M. Zhong, Y. He, Z. Liu, and Z. Li, Fingering instability in marangoni spreading on a deep layer of polymer solution, Phys. Fluids **32**, 112112 (2020).
[11] C. M. Bates, F. Stevens, S. C. Langford, and J. T. Dickinson, Motion and dissolution of drops of sparingly soluble alcohols on water, Langmuir **24**, 7193 (2008).
[12] S. Berg, Marangoni-driven spreading along liquid-liquid interfaces, Phys. Fluids **21**, 032105 (2009).
[13] A. Chandramohan, S. Dash, J. A. Weibel, X. Chen, and S. V. Garimella, Marangoni convection in evaporating organic liquid droplets on a nonwetting substrate, Langmuir **32**, 4729 (2016).
[14] A. I. Fedorchenko and J. Hruby, On the formation of dry spot in heated liquid films, Phys. Fluids **33**, 023601 (2021).
[15] S. Deodhar, S. P. Thampi, G. Madivala, and M. G. Basavaraj, Drops spreading on fluid surfaces: Transition from Laplace to Marangoni regime, Phys. Rev. Fluids **6**, L112001 (2021).
[16] J. G. E. Fraaije and A. M. Cazabat, Dynamics of spreading on a liquid substrate, J. Colloid Interface Sci. **133**, 452 (1989).
[17] J. F. Joanny, Wetting of a liquid substrate, Phys. Chem. Hydrodyn. **9**, 183 (1987).
[18] V. Bergeron and D. Langevin, Monolayer Spreading of Polydimethylsiloxane Oil on Surfactant Solutions, Phys. Rev. Lett. **76**, 3152 (1996).
[19] O. E. Jensen and J. B. Grotberg, Insoluble surfactant spreading on a thin viscous film: Shock evolution and film rupture, J. Fluid Mech. **240**, 259 (1992).
[20] L. Keiser, H. Bense, P. Colinet, J. Bico, and E. Reyssat, Marangoni Bursting: Evaporation-Induced Emulsification of Binary Mixtures on a Liquid Layer, Phys. Rev. Lett. **118**, 074504 (2017).
[21] C. Seyfert and A. Marin, Influence of added dye on Marangoni-driven droplet instability, Phys. Rev. Fluids **7**, 043602 (2022).
[22] K. Hasegawa and Y. Manzaki, Marangoni fireworks: Atomization dynamics of binary droplets on an oil pool, Phys. Fluids **33**, 034124 (2021).
[23] D. Lo Jacono, F. Plouraboué, and A. Bergeon, Weak-inertial flow between two rough surfaces, Phys. Fluids **17**, 063602 (2005).
[24] A. Hoang and H. P. Kavehpour, Dynamics of Nanoscale Precursor Film near a Moving Contact Line of Spreading Drops, Phys. Rev. Lett. **106**, 254501 (2011).
[25] M. N. Popescu, G. Oshanin, S. Dietrich, and A. M. Cazabat, Precursor films in wetting phenomena, J. Phys.: Condens. Matter **24**, 243102 (2012).
[26] O. Bäumchen, L. Marquant, R. Blossey, A. Münch, B. Wagner, and K. Jacobs, Influence of Slip on the Rayleigh-Plateau Rim Instability in Dewetting Viscous Films, Phys. Rev. Lett. **113**, 014501 (2014).
[27] Y. Wang and L. Bourouiba, Growth and breakup of ligaments in unsteady fragmentation, J. Fluid Mech. **910**, A39 (2021).
[28] N. Murisic and L. Kondic, On evaporation of sessile drops with moving contact lines, J. Fluid Mech. **679**, 219 (2011).

[29] A. Dominguez Torres, J. R. M. Intyre, J. M. Gomba, C. A. Perazzo, P. G. Correa, A. Lopez-Villa, and A. Medina, Contact line motion in axial thermocapillary outward flow, J. Fluid Mech. **892**, A8 (2020).

[30] Y. O. Popov, Evaporative deposition patterns: spatial dimensions of the deposit, Phys. Rev. E **71**, 036313 (2005).